Available online at www.sciencedirect.com
ScienceDirect
C. R. Physique 8 (2007) 845–864
COMPTES RENDUS PHYSIQUE
http://france.elsevier.com/direct/COMREN/

Neutron scattering/Diffusion de neutrons

High resolution neutron spectroscopy—a tool for the investigation of dynamics of polymers and soft matter

Michael Monkenbusch *, Dieter Richter

Institut für Festkörperforschung (IFF), Forschungszentrum Jülich, 52425 Jülich, Germany

Available online 8 November 2007

Abstract

Neutron scattering, with the ability to vary the contrast of molecular items by hydrogen/deuterium exchanges, is an invaluable tool for soft matter research. Besides the structural information on the mesoscopic scale that is obtained by diffraction methods like small angle neutron scattering, the slow dynamics of molecular motion on mesoscopic scale is accessible by high resolution neutron spectroscopy. The basic features of neutron backscattering spectroscopy, and in particular neutron spin-echo spectroscopy, are presented, in combination with illustrations of results from polymer melt dynamics to protein dynamics which are obtained by these techniques. ***To cite this article: M. Monkenbusch, D. Richter, C. R. Physique 8 (2007).***

Résumé

La spectroscopie de neutrons à haute résolution—un outil pour l'étude de la dynamique des polymères et de la matière molle. La diffusion de neutrons, avec la capacité de varier le contraste des molécules par l'échange hydrogène/deutérium, est un outil précieux pour l'étude de la matière molle. En plus de l'information structurale obtenue à des échelles microscopiques par les méthodes de diffraction comme la diffusion de neutrons aux petits angles, la dynamique lente des molécules est accessible par la spectroscopie de neutrons à haute résolution sur les mêmes échelles spatiales. Les principes de bases de la spectroscopie à rétro-diffusion, ainsi que la spectroscopie par écho de spin de neutrons, sont présentés dans cet article. L'apport de ces techniques est illustré par des exemples allant de la dynamique des fondus de polymère à celle des biomolécules. ***Pour citer cet article : M. Monkenbusch, D. Richter, C. R. Physique 8 (2007).***

Keywords: Soft matter; Neutron spin-echo; High resolution spectroscopy

Mots-clés : Matière molle ; NSE ; Spectroscopie haute résolution

1. Introduction

Neutron scattering (NS) is a versatile tool to investigate the link between macroscopic properties and structure and mobilities on the molecular scale. In the field of soft matter, much of the unique power of NS for this purpose, relies on the ability to exchange hydrogen by deuterium and thereby create a contrast even between otherwise chemically equal

* Corresponding author.
E-mail addresses: m.monkenbusch@fz-juelich.de (M. Monkenbusch), d.richter@fz-juelich.de (D. Richter).

1631-0705/$ – see front matter
doi:10.1016/j.crhy.2007.10.001

(macro)molecules in the sample. See e.g. the seminal experimental proof of the random Gaussian chain conformation of linear polymers using small angle neutron scattering (SANS) [1–3]. Beyond the structural 'snap shots' provided by diffractometer experiments—predominantly SANS for soft matter—the mechanical and flow properties depend on molecular mobilities and constraints of motion. The corresponding information is contained in the inelastic spectrum (mostly quasielastic broadening) of the scattered intensity, i.e. a spectral analysis of the SANS intensity is needed to analyze the mode of motions of a linear macromolecular coil or any other mesoscopic molecular assembly. Due to the mesoscopically large objects and the corresponding typical length that must be traveled by the scattering molecular parts, in order to be visible in the low wave vector Q, SANS range, the involved relaxation rates correspond to energy transfers in terms of quasielastic spectral broadening that are many orders of magnitude smaller than the kinetic neutron energies. Spectroscopic neutron instruments that are able to enter this domain need energy resolutions below 1 μeV down to neV. The simple example of a mesoscopic sphere of 100 Å diameter diffusing in water may illustrate this. The Einstein–Stokes diffusion coefficient

$$D = \frac{k_B T}{6\pi\eta R} \tag{1}$$

for such a sphere with radius $R = 5 \times 10^{-9}$ m in water with the viscosity $\eta = 10^{-3}$ Ns/m^2 at $T = 300$ K is $D = 4.4 \times 10^{-11}$ m^2/s. At a scattering vector that is adapted to the size of the sphere, e.g. $Q = \pi/R$, a quasielastic broadening of $\Delta E = 11$ neV, equivalent to $\tau(Q) = 1/Q^2 D = 59$ ns, results. Even in a medium as liquid as water, the observation of motions on the mesoscopic scale, which is the important one for the understanding of soft matter, requires extreme spectroscopic resolution compared to the typical cold neutron energy around 1 meV. Even the diffusion of water molecules at this low Q-value yields a relaxation time of $\simeq$1 ns or $\Delta E \simeq 0.7$ μeV which is well in the neutron spin echo (NSE) range and marginal for backscattering!

In general, the neutron signal from the dynamics in soft-matter corresponds to some kind of Brownian motion. Simple diffusion, such as in the above example, is the most simple case. Besides the random thermal forces, the relaxation motion is governed by the equilibrium between hydrodynamic friction and couplings and elastic forces that often stem from entropic effects.

Another field of interest in polymers and soft matter pertains to the fact that many polymers undergo the transition from melt to solid not by crystallisation but via a glass transition. Here a very broad range of lengths and times are of interest. In particular, the intermolecular distance—typically around 5 Å—sets the length scale. The characteristic times freeze in the course of the glass transition upon cooling from sub-ps to macroscopic. Neutron investigations of this type of relaxations require intermediate Q and the largest available dynamic range.

2. Instrumentation

In the following we will discuss neutron spin echo and backscattering spectroscopies which provide the energy resolution that enables the observation dynamics in soft condensed matter samples on the important mesoscopic scale given by the size of (macro)molecules and molecular aggregates. Fig. 1 indicates the spatio-temporal range that may be covered using these methods.

2.1. Backscattering spectrometers (BSS): from 0.7 to 30 μeV (20 ps . . . 1 ns)

Backscattering spectrometers achieve their resolution of $\Delta E/E_0 \simeq 3 \times 10^{-4}$ by employing perfect crystals (e.g. silicon wafers) at incident angles close to 90° where the Bragg reflected wavelength is insensitive up to 2nd order of the deviation from exact backscattering. The intensity loss due to the narrow wavelength filtering is compensated by the use of the large divergence of the incoming beam and huge solid angle coverage by the detectors. The latter is achieved by focusing analyzer mirrors covered with crystal (silicon) platelets that map the sample on a detector. The energy scan is effected by a driven motion of the monochromator crystal arrangement which Doppler shifts the neutron velocity [4,5].

A broad incoming divergence is obtained by the use of a phase space transformer (fast perpendicular to **Q** moving mosaic crystals) that feeds a large area focusing perfect crystal monochromator assembly on the Doppler drive [6–8].

The salient features of this BSS setup is shown in Fig. 2. A neutron beam (NB) with divergence of $\simeq$1° and a wavelength width of $\Delta\lambda/\lambda \simeq 0.1$, as prepared by a velocity selector, enters the spectrometer and hits a moving

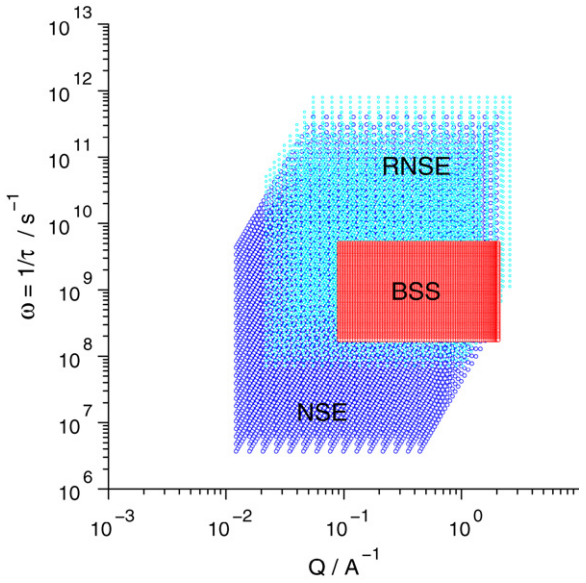

Fig. 1. Indication of the (Q, ω)-domains which may be covered by the high resolution spectroscopic neutron scattering methods discussed in this article. Note that the spin-echo methods yield the Fourier transform of $S(Q, \omega)$ and the direct measurement for the vertical scale is the Fourier time, $\tau = 1/\omega$, whereas for BSS the data are obtained as spectra $S(Q, \omega)$. Other neutron spectroscopies (time-of-flight, three axis) extend in the region beyond BSS into the upper right of the figure.

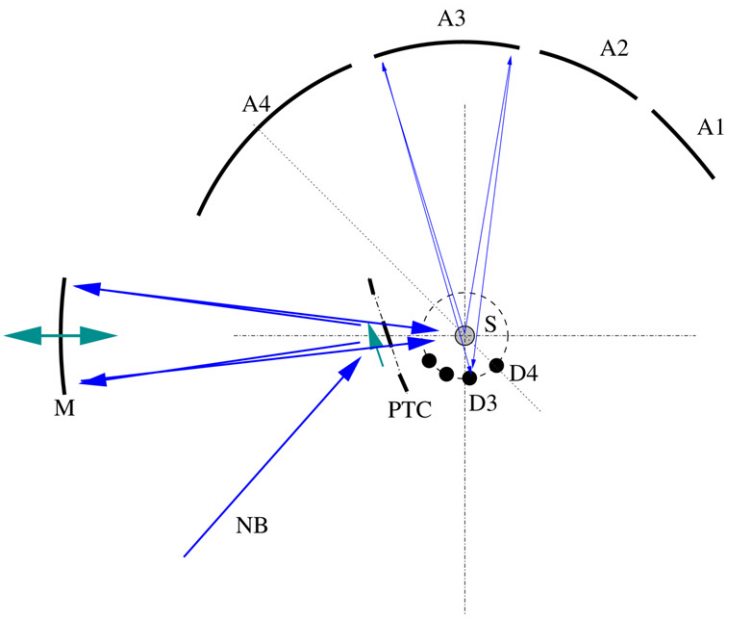

Fig. 2. Schematic setup of a backscattering spectrometer with phase space transforming chopper (PTC).

mosaic crystal (pyrolytic graphite) on the wheel of the phase space transforming chopper (PTC). Due to the movement of the differently oriented crystallites in the mosaic, the beam profile is transformed such that the divergence increases at the expense of the wavelength width. The beam, thus prepared, suits the acceptance of the Doppler monochromator (M) where the neutrons are reflected by perfect Si-wafer crystals in backscattering geometry. Wavelength variation within the percent range is effected by oscillatory linear (Doppler) movement of the monochromator in

the beam direction. After the time-of-flight of a bunch of neutrons from the PTC crystal to the monochromator and back to the PTC, the wheel moves such that a neutron transparent window replaces the pyrolytic graphite crystal and the monochromatized beam can hit the sample (S). Neutrons scattered from the sample reach one of the large scale focussing Si-analyzer plates (A1–A4). Neutrons with the right wavelength are backscattered and focussed on the associated detector tube (D1–D4). Neutrons scattered by the sample directly into the counting tubes are discriminated by their different time-of-flight. Correlating Doppler velocity and arrival of the neutrons as a function of time in the counting electronics yields the energy transfer spectrum. Note that for clarity only 4 angles instead of typically 16 scattering angles are shown and any shieldings and beam stops that are essential to control background are omitted.

Due to the resolution properties in energy and wavevector, the BSS is used to cover the intermediate to large Q-range from about $0.2, \ldots, 2\ \text{Å}^{-1}$. Pertaining soft matter this is particular suited to investigate glass forming systems. On the low Q-side it covers the high Q-tail of the generic polymer dynamics which is dominated by chain connectivity. However, the ability to contribute to the exploration of diffusion and internal motion of biological molecules, is largely in its infancy. The measured signal in the majority of cases is dominated by incoherent scattering from protons. Thus the local dynamics as expressed in the self correlation functions of molecular segments is measured.

2.2. Neutron spin-echo spectrometers, from ps to μs (0.7 neV . . . 0.7 meV)

Complementary to backscattering spectrometers and extending the energy time domain by up to 3 further orders of magnitude are neutron spin-echo (NSE) spectrometers. NSE spectrometers use velocity dependent polarisation modulation to prepare a neutron beam prior to scattering and to decode the scattered radiation [9–11]. The combination of preparation and decoding allows for the detection of miniscule velocity changes and energy transfers, respectively, during scattering. The final polarisation of the detected neutrons carries the information on inelastic scattering processes. If no velocity change occurs the full polarisation is recovered after the decoding step—irrespective on the initial neutron velocity—an effect which is called spin-echo and coins the name of the method. It bears some analogy with the spin-echo observed in NMR spectroscopy [12]. However, in neutron spin-echo spectroscopy (see Fig. 3), the intermediate depolarisation is caused by the velocity distribution of the incoming neutrons, and the finally restored polarisation is a measure of individual velocity changes suffered by the neutrons in the scattering process and NOT connected to spin relaxations in the sample, as in NMR.

It is important to note that the spin manipulation in NSE is only a means to analyze energy transfers similar to the role of crystal analyzers in BSS. The very high resolution at high intensity results from the decoupling of the sensitivity to detect a very small energy transfer compared to the width in energy or velocity of the neutrons. Each neutron spin serves as individual stop watch for only this neutron. However, the NSE technique does not yield the

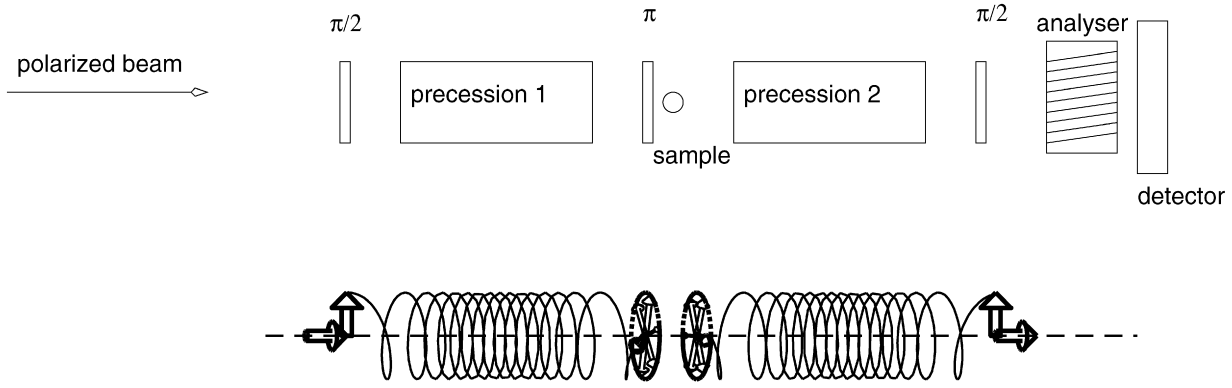

Fig. 3. Schematics of a generic NSE instrument. In the classical IN11 type spectrometers the precession zones are realised by solenoids that create a longitudinal magnetic field. The flippers are rectangular flat coils with (e.g.) vertical axes that rotate the neutron spins after the neutrons entered through the Al wire of the winding until they leave the flipper at the other side. The spin precession is indicated in the lower half of the figure.

scattering function $S(Q,\omega)$, which directly relates to the double differential wave vector and frequency dependent scattering cross-section, but its Fourier transform, the intermediate scattering function:

$$S(Q,t) = \int_{-\infty}^{\infty} \cos(\omega t) S(Q,\omega)\,\mathrm{d}\omega \tag{2}$$

where it is assumed that—for soft matter problems—in the relevant regime $\hbar\omega \ll k_B T$ and $S(Q,\omega) = S(Q,-\omega)$.

2.2.1. High resolution solenoid type NSE

The generic IN11 type high resolution NSE spectrometers need a solenoid around the beam path to prepare the neutron spins and a symmetric solenoid in the decoding secondary scattering arm of the spectrometer. The coding/decoding magnetic field sections are limited by spin-flippers. The first $\pi/2$-flipper rotates the neutron spin from an axial direction to a perpendicular orientation such that the Larmor precession starts. Time evolution occurs in the first solenoid where a many turn Larmor precession takes place. The exact precession angle depends on the time the neutron stays inside the solenoid field (i.e. it is inversely proportional to its velocity). Close to the scattering point (the sample) a π-flipper reverses the accumulated precession angle to its negative value. After the scattering process the precession continues in the second solenoid until the obtained polarisation is 'frozen' by the second $\pi/2$-flipper. An analyzer transmits the neutrons according to their axial spin projection, i.e. the transmission is $T = (1+\cos(\alpha))/2$ where α is the finally accumulated precession angle. If the setup is symmetric and the neutron velocity was not changed $\alpha = 0$—independent of the starting velocity—otherwise part of the polarisation is lost. After some mathematics one arrives at the following approximate expression for the detected intensity:

$$I_{\mathrm{Det}} \propto \frac{1}{2}\left[S(Q) \pm \frac{\exp(-\Psi^2)}{Z}\cos\left(\delta\gamma\frac{m_n}{h}\lambda\right)\int \cos\left(J\lambda^3\gamma\frac{m_n^2}{2\pi h^2}\omega\right)S(Q,\omega)\,\mathrm{d}\omega\right] \tag{3}$$

where $t = J\lambda^3\gamma m_n^2/(2\pi h^2)$ is the Fourier time with $\gamma \simeq 183.033\times 10^6\ \mathrm{s^{-1}\,T^{-1}}$ the Larmor precession coefficient of the neutron, m_n the neutron mass and $J = \int |B|\,\mathrm{d}l$ the magnetic field integral along the path from $\pi/2$-flipper to π-flipper, i.e. along the path through one of the velocity encoding precession spaces. $\delta = J_1 - J_2$ is the asymmetry of the field integral between both spectrometer arms. Under the idealising assumption that the incoming wavelength distribution and the distribution of field integrals around their nominal values are Gaussians, the following explicit relations hold: $Z^2 = 1 + 4\Sigma^2\Lambda^2\gamma^2 m_n^2/h^2$ and $\Psi^2 = [\Sigma^2\lambda^2 + \Lambda^2\delta^2]\gamma^2 m_n^2/h^2/Z^2$. $\Sigma^2 = \langle\Delta J^2\rangle/2$ relates to the field integral inhomogeneity and $\Lambda = \Delta_{\mathrm{FWHM}}\lambda/4/\sqrt{\ln 2}$ to the full width at half maximum (FWHM) of the incoming wavelength distribution. For 10% wavelength width with respect to the mean wavelength $\lambda = 1$ nm, $\Sigma = 2\times 10^{-6}$ Tm and $\delta = 0$, these typical numerical values are obtained: $Z = 1.0015$, $R = \exp(-\Psi^2) = 0.43$.

In an experiment, in the first instance, the asymmetry δ is varied in order to determine the amplitude, A, of the first cosine factor in Eq. (3):

$$A = \pm\underbrace{\exp\left(-\Psi^2\right)/Z}_{=R}\int \cos\left(\underbrace{J\lambda^3\gamma\frac{m_n^2}{2\pi h^2}}_{=t}\omega\right)S(Q,\omega)\,\mathrm{d}\omega \tag{4}$$

i.e. up to the factor R the amplitude A is proportional to the desired value of $S(Q,t)$. Usually it is normalised by dividing by $S(Q)$, which removes all normalisation factors (like detector sensitivity, ...) from the result. The resolution factor R may be determined by measuring a reference sample with $S(Q,t)/S(Q) = 1$ and then be used to correct the echo amplitude equation (4) by dividing it out.

The technique has the potential to reach Fourier times of the order of 1 μs, corresponding to an energy resolution of 0.7 neV. Currently the IN15 instrument at the ILL operates routinely with Fourier times up to 200 ns. Seven of these instruments are currently operated or under construction world wide: IN11, IN15 (ILL) [13,14], J-NSE (JCNS, FRMII) [15], NG5-NSE (NIST) [16], C2-2 (JRR3, Tokai) [17,18], SNS-NSE (JCNS, SNS under construction) [19–21].

2.2.2. Wide angle NSE

The operation principle of wide angle spin echo spectroscopy, as first realised by the SPAN instrument at HMI [22], is basically the same as that of the generic IN11 type spectrometers. The difference between both (SPAN and IN11)

consists in a different realisation of the precession magnetic field, in order to be able to simultaneously use a broad range of scattering angles. The magnetic field is rotationally symmetric around the sample position in the scattering plane. The field direction is radial, pointing to or from the sample position. The latter is realized by a pair of ring coils below and above the scattering plane that are operated to produce reverse field directions. The combination of their fields is zero at the central sample position and increases with radial distance. SPAN is build such that it can produce a field integral on any radial path that is about $1/10 \cdots 1/20$ of the current solenoid type spectrometers.[1] Once a sufficient number of analyzers is available, this type of spectrometer may cover scattering angles from nearly 0° to nearly 180° simultaneously. The only limitation is given by the investigated physical effects that typically show relaxation rates $\Gamma(Q) \propto Q^{2\cdots4}$ such that for one magnetic field setting only a small part of the Q-range is within the window, where relaxations lead to observable effects in $S(Q,t)$. However, especially at larger scattering angles, the relative variation of Q in an angular sector of given width is not so large that the dynamic range becomes too imbalanced. In that case, the coverage of a complete angular sector leads to significant intensity gains. Thus, the main application of this type of NSE spectrometer is in the field of glass physics and magnetic fluctuations that, however, are beyond the scope of this article.

2.2.3. Zero field NSE

Zero field or resonance NSE [23] relies on the same principles of spin velocity encoding and yields the same type of information as the previously described NSE spectrometers. However, whereas in the 'normal' NSE setup the velocity to spin rotation angle encoding happens due to Larmor precession in a magnetic field between static flippers, in zero field NSE the spin direction is preserved—due to zero magnetic field—in the neutron flight paths. Time-of-flight and velocity coding in this case are effected by rotating flipping fields, where the relative phase angle between start and arrival at the flippers that limit the flight path, determines the final spin direction.

Two instruments that may be used for the investigation of soft matter dynamics are the RNSE at the LLB and RESEDA at the FRMII. These instruments are also equipped with a very low field conventional NSE option that takes advantage of the μ-metal shield around the beam path. In combination with the use of lower wavelengths this option allows for the extension of the time range towards very small values in the sub-ps range [24,25]. Limitations of the zero field techniques are currently given by the technical challenge of building the flippers. They have to provide the required high internal magnetic fields and must be transparent to neutrons. They have to show low parasitic scattering and to possess the required mechanical accuracy. In addition the beam geometry implies length inhomogeneities that restrict the acceptable beam divergence.

Specific advantages of the existing installations are the large Q-values that can be measured, which qualifies them for glass dynamics investigations. Also some aspects of the dynamics of biomolecules have been successfully treated [26,27].

3. Polymer melts

3.1. Motion of the rouse chain

A starting point to classify and assess the scattering $S(Q,t)$ from a polymer chain is the comparison with the predictions of the standard model for polymer dynamics, the Rouse model, which first was developed to explain viscoelastic behaviour [28]. Later De Gennes gave a computable expression for the scattering function [29]. The model assumes a Gaussian chain of beads that are connected by entropic springs and interact with their environment solely via a simple friction against the homogeneous non-moving background and random forces from the heat bath. The solutions of the equation of motion are cosine-type relaxation modes along the topology of the chain and with a relaxation rate proportional to the square of the mode number p, $1/\tau_p = p^2/\tau_R$ with $\tau_R = \zeta N^2 l^2/(3\pi^2 k_B T)$ with $Wl^4 = 3kTl^2/\zeta$ (ζ: segmental friction coefficient, l: segment length). For a detailed derivation see Ref. [30]. Including centre-of-mass motion, the structure factor of one single chain is:

$$S(Q,t) = \exp\bigl(-Q^2 Dt\bigr) S_{\text{chain}}(Q,t) \tag{5}$$

[1] The WASP project of ILL aims at a field integral comparable to the current maximum integral of the IN11 solenoid spectrometer, i.e. an order of magnitude beyond that of SPAN.

with the diffusion coefficient $D = k_B T/(N\zeta)$ and

$$S_{\text{chain}}(Q,t) = \frac{1}{N}\sum_{n,m}\exp\left(-\frac{1}{6}Q^2\left[|n-m|l^2 + \Phi^1_{nm}(t)\right]\right) \tag{6}$$

with

$$\Phi^1_{nm}(t) = \frac{4Nl^2}{\pi^2}\sum_{p=1}\frac{1}{p^2}\cos\left(\frac{p\pi m}{N}\right)\cos\left(\frac{p\pi n}{N}\right)\left[1-\exp(-tp^2/\tau_R)\right] \tag{7}$$

$S(Q,t=0) = S(Q)$, i.e. the structure factor corresponds to a snap-shot of the chain structure: replacing the summations by integrals and observing the relation $R_g^2 = \frac{1}{6}Nl^2$ for the radius-of-gyration, Eq. (6) immediately leads to the well-known Debye-function

$$S(Q) = N f_{\text{Debye}}\left(Q^2R_g^2\right) \tag{8}$$

$$f_{\text{Debye}}(x) = \frac{2}{x^2}\left(\mathrm{e}^{-x} - 1 + x\right) \tag{9}$$

The single segment scattering function for an inner chain segment—as may be measured by incoherent scattering—can be derived from Eq. (6) by setting $m = n = N/2$ and replacing the p-summation by an integral:

$$S_{\text{inc}}(Q,t) = \exp\left(-\frac{1}{6}Q^2\sqrt{\frac{12k_BTl^2}{\pi\zeta}}\sqrt{t}\right) \tag{10}$$

For long (infinite) chains, the resulting $S_{\text{chain}}(Q,t)$ has a characteristic scaling form [29,31,30]:

$$S_{\text{chain}}(Q,t)/S(Q) = F\left(Q^4\frac{Wl^4}{36}t\right) \tag{11}$$

$F(x)$ is the dynamic structure factor due to de Gennes [29]

$$F(x) = \int_0^\infty \mathrm{d}u\exp\left[-u - x^{1/2}h(u/x^{1/2})\right] \tag{12}$$

with

$$h(y) = y\,\mathrm{erf}(y/2) - y + \frac{2}{\sqrt{\pi}}\exp\left[-(y/2)^2\right] \tag{13}$$

In the limit of very long chains the center-of-mass diffusion is negligible and omitted here. Then the only parameter Wl^4 is a combination of bead friction and average bond length, which is independent of the chosen model decomposition of the polymer chain into a certain number of beads connected by springs comprising a certain number of chain segments. The function may be fairly approximated by $F(x) \simeq \exp[-(x/2.7)^{0.7}]$. Deviations from the scaling implied by Eq. (11) with its relaxation rate $\propto Q^4$ indicate effects beyond the Rouse model.

In spite of the simplicity and age (half a century), the Rouse model serves as reference against which experimental results may be tested to identify new physical effects.

The following examples illustrate on the one hand the effects of chain-chain interactions that lead to 'entanglements' and the degree of detail on the motion that can be obtained by a combination of high resolution NSE and selected chemical modification of a polymer melt system. On the other hand, the deviations due to specific intrachain potentials are shown. Finally, the combination of NSE experiments and molecular dynamics calculation shed light on the limits of the validity of the Rouse model (Fig. 4).

3.2. Entanglements, reptation: motion in a tube and beyond

Peculiarities in the viscoelastic properties of linear polymer melts (and solutions), like the observation of a rubber elastic regime over a range of intermediate frequencies or the chain length dependence of viscosity or diffusion, are indications of the effect of entanglements. These have been observed half a century ago and were already then

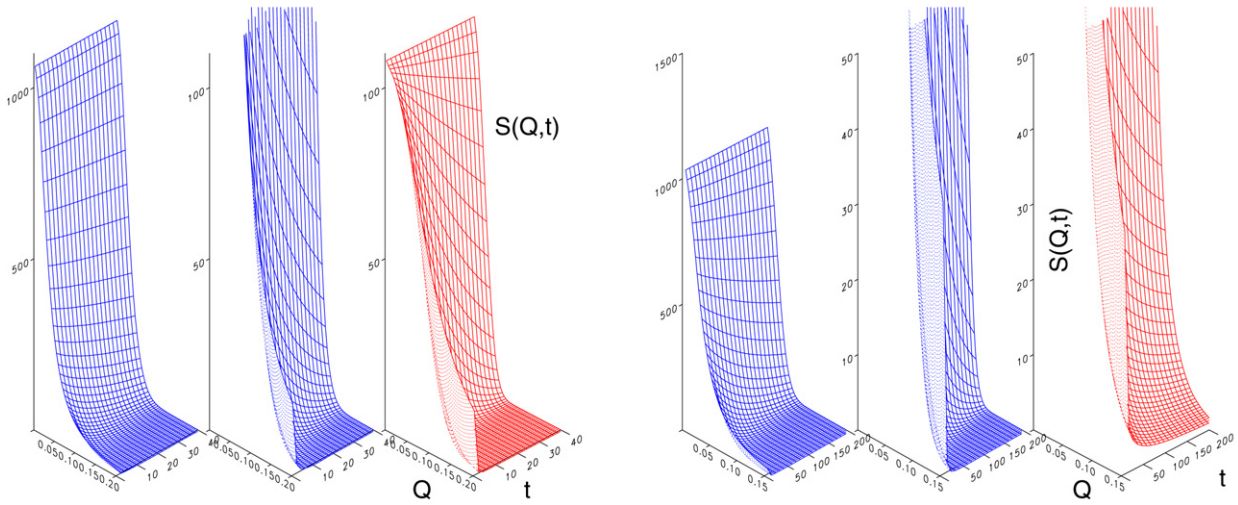

Fig. 4. Rouse $S(Q,t)$ for different chain lengths (left) and the influence of entanglements on $S(Q,t)$ (right).

associated with entanglements [32,33], but a quantitative microscopic understanding only emerged form the work of de Gennes and Doi and Edwards in the late 1970s. In order to explain the associated effects, they developed models that view the chain as confined in a tube and performing 'reptation' motion within this tube [34–42]. The explanation of the effects with the above model requires the introduction of a length scale $a = d$ [37], which pertains to the diameter of the virtual tube around the polymer chain under consideration.

The pure Rouse model exhibits no length scale in its validity regime of intermediate Q which is limited by the finite length of the polymer chain, i.e. a finite coil radius of gyration R_g, on the one side and the segment size on the high Q side. Now, the entanglement formed tube constraint adds a new length scale to the framework of the ideal Rouse model. This length scale may be interpreted as tube diameter d. It is also the step length of the random walk that defines the contour of the tube a.

$$\frac{S(Q,t)}{S(Q)} = \big(1 - F(Q)\big)\exp\left(\frac{t}{\tau_0}\right)\operatorname{erfc}\big(\sqrt{t/\tau_0}\big) + F(Q)S_{\text{escape}}(M_w, d; Q, t) \tag{14}$$

where $F(Q) = \exp[-(Qd/6)^2]$ is the (cross-sectional) form-factor of the tube and M_w the molecular weight of the polymer. At very short times (here below a few ns) the segment diffusion is still not yet affected by the tube constraints. Only after the 'entanglement time' τ_e, the segment displacement suffices to probe the existence of the virtual 'walls' of the tube. This short time regime is not explicitly contained in Eq. (14). The two time scales in Eq. (14) are given by $\tau_0 = 36/(Wl^4Q^4)$ for the local reptation due to Rouse type segment diffusion along the tube and $\tau_d = 3N^3l^2/(\pi^2 Wd^2)$ for the reptation type escape of the chain from the tube. Wl^4 is the Rouse rate, known from previous experiments [43], and $N \propto M_w$ the number of segments per chain (here $N \simeq 13\,000$). Due to $\tau_d \simeq$ ms, the tube escape term S_{esc} is virtually constant for the high M_w polyethylene (PE) in the accessible NSE time range ($t < 200$ ns).

Neutron scattering allows one to test the model scenarios on a molecular level. Whereas for short times during which the segment displacement is less than d, the Rouse $S(Q,t)$ still holds, at longer times, deviations become visible [44,45]. The full effect of the tube constraint, however, only became accessible after the IN15 NSE instrument at ILL extended the Fourier-time range to several 100 ns through the use of very long wavelength neutrons [46]. The thus obtained data show a clear Q-dependent plateau towards larger times where the relaxation, i.e the decay of $S(Q,t)$ virtually comes to a stop (Fig. 5). If the average chain segments probed all motions allowed by the topological constraints that result in the model tube, no further time dependence of $S(Q,t)$ is visible and the Q-dependent level corresponds to the scattering of the thick smooth average tube instead of the chain scattering proportional to a Debye function as seen in SANS. In a way, this effect is analogous to the elastic incoherent structure factor (EISF)—i.e. the relative intensity $I_{\text{EISF}}(Q)$ of the component with no detectable spectral broadening ($\simeq I_{\text{EISF}}(Q)\delta(\omega)$)—in spectroscopy experiments, e.g. using a TOF spectrometer. The Q-dependence of the elastic intensity corresponds to

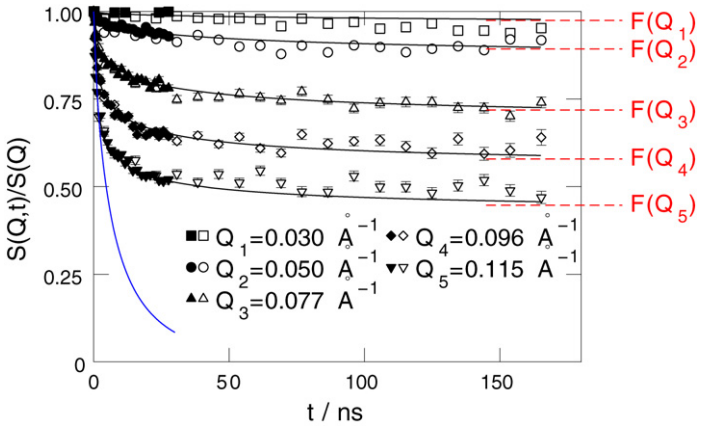

Fig. 5. NSE relaxation curves from fully entangled polyethylene $M = 190$ kg/mol compared to the Rouse prediction (blue line) and de Gennes model (black lines) Eq. (14) with $d = 48$ Å which directly may be inferred from the Q-dependence $F(Q) = \exp(-Q^2 d^2/36)$ of the plateau values.

the probability density of the (proton) position after a long observation time. The exact shape of $S(Q,t)$ as given in Ref. [46] allows the discrimination between various proposed models for the entangled chain motion in favour of the reptation scenario of de Gennes [34,35] which correspond to the tube model of Doi and Edwards [37–42]. The extra length scale a is identified with the tube diameter $d \simeq 48$ Å for the investigated polyethylene melt with a molecular weight of $M_w = 36$ kg/mol. The tube model explains the 'plateau' of the viscoelastic modulus and yields a plateau value of [47,48]

$$G_N^{(0)} = \frac{4}{5}\frac{\rho N_A k_B T}{M_e} = \frac{4}{5}\frac{\langle R_e^2\rangle}{M}\frac{\rho N_A k_B T}{d^2} \tag{15}$$

with N_A Avogadro's number, M the molecular weight of the polymer with a root-mean-square chain end-to-end distance R_e, ρ the mass density, d the tube diameter corresponding to an 'entanglement molecular weight' $M_e = Md^2/R_e^2$. Here still a factor of $\simeq$1.5 between rheologically derived tube diameter and the NSE value is encountered. Given the still very limited number of polymers analyzed by NSE, it is not yet clear whether this factor is 'universal' or depends on chemical details, e.g. local stiffness.

The limiting behaviour of $S(Q,t)$ of the reptating chain towards large molecular weights is virtually reached at $M_w = 36$ kg/mol as exploration of the M_w dependence up to 190 kg/mol showed [49]. Incoherent scattering [50] of the initial short time interval below the entanglement time τ_e and above τ_e, where the segments start to 'feel' the tube constraint, reveal the predicted transition from the Rouse prediction of segmental diffusion, i.e. $\langle r(t)^2\rangle \propto t^{1/2}$ below τ_e and $\langle r(t)^2\rangle \propto t^{1/4}$ in the local reptation regime just above τ_e. Also, here, the textbook [30] prediction of the reptation scenario is corroborated.

Thus in a next level of NSE exploration of polymer dynamics in the reptation regime of de Gennes expression that fits the reptating large M_w chain may serve as reference to identify the consequences of more subtle effects of the reptation scenario, known as 'contour length fluctuations', CLF and 'constraint release', CR [47]. CLF pertains to additional loss of constraints associated with the fluctuating retractions and extensions of the chain ends. The pure reptation model assumes diffusion of the chain along the tube contour. Finally this causes the chain to leave the initial tube completely. Thus it determines the relaxation at long times and leads to a normal centre-of-mass diffusion that happens beyond the observation window of NSE spectroscopy. CLF adds a faster relaxation effect the importance of which scales with the concentration of ends, i.e. it becomes important for shorter chains. Likthman and McLeish gave a closed expression for the effect of CLF on $S(Q,t)$ in the plateau regime [51] that explains deviations of $S(Q,t)$ as observed at smaller but still fully entangled chain length.

From scaling arguments and model simulation they arrive at the time dependence $s(t) = 0.75 M_e/M[t/\tau_e]^{1/4}$ by which the ends of the undisturbed ($t = 0$) tube recede due to CLF, see Fig. 6. After a retraction the chain comes out of the residual tube on a new path—indicated by the broken lines in Fig. 6. The larger the renewed contour, the longer waiting time needed for s to proceed, which is described by the $\propto t^{1/4}$ time dependence of $s(t)$. Using the standard Gaussian path expression for the pair distribution of any segments $m, n\langle r^2\rangle = a^2|m-n|$ and counting a topological

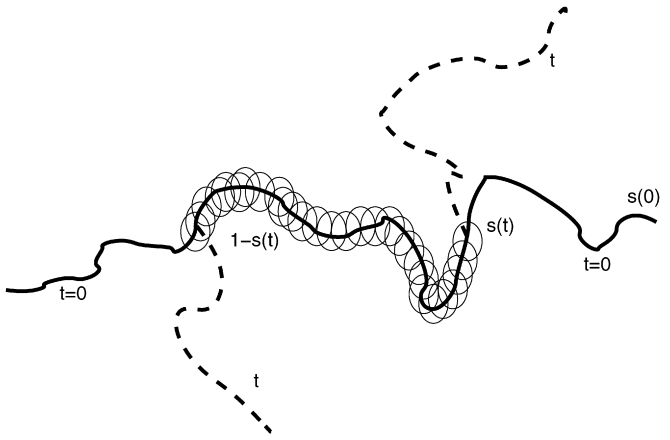

Fig. 6. Sketch indicating the CLF process. After time t the tube is only conserved in the central chain part, the ends up to a relative end-distance along the contour of $s(t)$ respectively $1 - s(t)$ are displaced (solid vs. dashed).

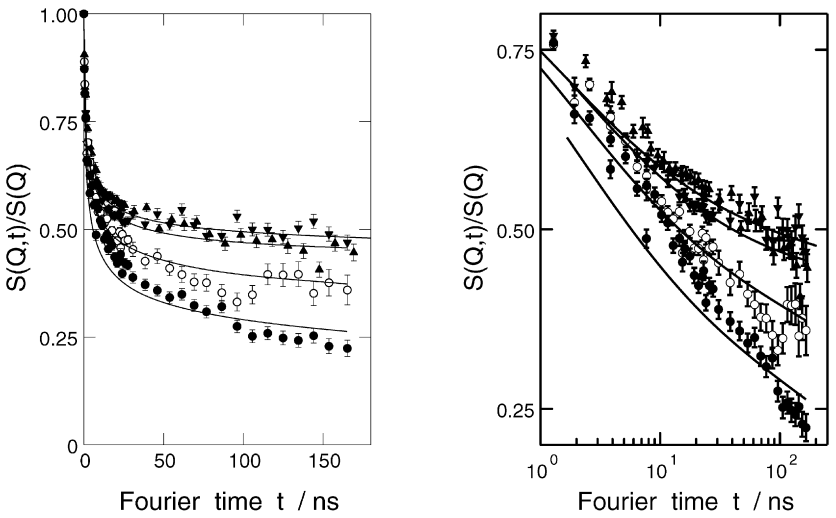

Fig. 7. NSE relaxation curves from fully entangled polyethylene for $M = 190$ (triangle down), 36 (triangle up), 16 (open circle), 12 (close circle) kg/mol for $Q = 0.115$ Å^{-1}. Lines correspond to prediction of Eqs. (14) and (16). For the lowest molecular weight, deviations become obvious.

distance between original and renewed tube end segments by connection via the time dependent bifurcation point $s(t)$, Likthman and McLeish [52] arrived at

$$S_{\mathrm{esc}}(Q,t) = \frac{N}{2\mu^2}\left(2\mu + \mathrm{e}^{-2\mu} + 2 - 4\mu s(t) - 4\mathrm{e}^{-2\mu s(t)} + \mathrm{e}^{-4\mu s(t)}\right) \tag{16}$$

with $\mu = Q^2 N l^2/12$ ($N =$ number of segments with length l) and M_e is the entanglement molecular weight and $\tau_e = \tau_r (M_e/M)^2$ the entanglement time. Assuming Gaussian chain statistics, this leads to the simple analytic expression (16) [51,53]. The curves in Fig. 7 are computed by using Eq. (16) in Eq. (14) without the introduction of any new parameter beyond the tube diameter d which keeps the value that has been obtained for high M_w.

By deuterium labelling of the chain ends of the scattering chain—here with a hydrogenated center section only—in a melt of deuterated chains, the scattering of the ends could be suppressed and thereby the CLF-relaxation were made invisible. The remaining dynamics of the inner chain part well confined in the tube is identical to that of the $M \to \infty$ limit of $S(Q,t)$ [54]. The observation of this behaviour is a strong evidence for the correctness of the interpretation of the extra relaxation in the plateau regime as observed in Ref. [51] as associated with the ends, i.e. 'contour length

fluctuations'. This gives a further a posteriori justification of the explanation of the $\eta \propto M^{3.4}$ instead of the pure reptation prediction $\propto M^3$ as an effect of CLF [55].

However, there is a second effect that lifts tube constraints, an effect that is anticipated as 'constraint release', CR. Constraint release occurs along the tube if a confining neighbour chain moves away laterally. While CLF could still be modeled—in the spirit of a mean field approach—as a single chain phenomenon, CR is a genuine many body effect, making its modeling more difficult. In order to make this effect visible within the NSE regime, the molecular weight (of the confining chains) has to be further reduced. It is obvious that the behaviour—as seen in terms of the single chain structure factor $S(Q,t)$ as far as NSE is involved—must change from the reptation reference with extended plateau levels for large molecular weights to the 'reference' Rouse dynamics if the molecular weight becomes low enough. In order to focus on the effect of the tube forming chains on constraint release, in a recent series of experiments, the dynamics of a long labelled chain in a matrix of successively shorter PE-chains has been investigated [56]. In the limit of very short chains in the surrounding melt, even the long observed chain exhibits Rouse dynamics, gradually deviating from it and approaching the reptation features upon increasing the molecular weight of the surrounding melt. Unfortunately there is no closed expression currently available to describe the scattering function in the regime of intermediate matrix chain lengths. Nevertheless, a slip link model [57] that has to be solved by simulation, is able to reproduce the salient features of the observed scattering functions in the transition regime. The model describes the tube constraints by a number of slip links that may glide along the chain and are anchored by springs to the embedding space. The CR effect is modelled by coupling the loss of a slip link at the end of one chain to the removal of a slip link from another chain of the simulated ensemble at a random position. The bead spring chains are simulated in the framework of Brownian dynamics.

The development of entanglements and the associated reptation scenario largely depend on topological interaction and constraints that result from them. Besides the friction and entropic springs from the Rouse model, only the effective tube diameter and the chain length influence the viscoelastic and scattering results.

Further architectures beyond linear chains and bimodal blends of these, show further new effects that pertain to the chain topology and the above regime of physical interactions. Whereas the viscoelastic effects may be huge, e.g. if a linear chain with a 3-arm star of the same size is compared [47], the observable changes in neutron spectra are less spectacular. However, future investigations towards this line—in particular when the new instruments with extended Fourier time range become available—will further test and discriminate concepts and models on a molecular scale.

3.3. Validity of the Rouse model concepts

It is still astonishing that—despite its ultimate simplicity—the Rouse model is so successful to describe the salient feature of polymer dynamics and, together with directly imaginable severe topological constraints, suffices to describe the reptation regime. All interactions with the other chains in the melt are lumped into one single friction parameter, the value of which must be determined by the experiment. The question of the nature of this friction generating interaction with the other chains and the validity of the mode concept has been addressed with the help of molecular dynamics calculations (MD) [58–62]. For short polymer chains a realistic MD calculation that covers the time range of several ns, over which NSE observes the Rouse relaxations, was possible. The computations were verified by comparison with NSE results. Closer inspections reveal differences as well between MD and NSE results from the Rouse model prediction. Also the centre-of-mass diffusion has been found as slightly sublinear in this time regime: $\langle r(t)^2 \rangle \propto t^{0.8}$ in the MD results, which are corroborated by the NSE data. The MD data allow insights into the motional details that are unavailable by direct analysis of the scattering results. Besides the modified centre-of-mass diffusion, the analysis reveals that the Rouse modes that imply exponential decay of correlators with a rate proportional to p^2—where p denotes the mode number—become stretched exponentials for the higher modes. The stretching exponent drops to $\beta = 0.75$ at $p = 10$ for the investigated chain length of 30 repeat units polybutadiene [62]. Comparing a direct way to compute $S(Q,t)$ with a route that implies the assumption of Gaussianity of the segmental displacement distributions—as in the derivation of the Rouse model functions—the non-validity of this approximation is identified as the primary reason for the observed deviation between the Rouse model prediction and the MD and NSE data. The friction itself came out quite close to the experimental value, however, not yet perfect since a scaling factor of 0.8 from the time scale was required to match NSE and MD results.

4. Solutions, gels and microemulsions

4.1. Hydrodynamic coupling: the Zimm model

The dynamics of a Gaussian chain in dilute solution is quite different from the chain dynamics in a melt as described by the Rouse model. The difference is explained by the dominance of hydrodynamic coupling between segments. The flow induced by a force exerted on one segment leads to a force onto another chain segment that is immersed in the flow. The coupling may be described by the Oseen tensor and leads to a mode spectrum of relaxation rates $\propto p^{3/2}$ instead of $\propto p^2$ in the Rouse case. It finally results in the structure factor for Zimm dynamics that can be cast into a master function $S(Q,t)/S(Q) = F(Q^3 tkT_B/[6\pi\eta]) = F(\tilde{\Gamma}(Q)t)$ with an universal function $F(x)$ [30,63,31]:

$$F(x) = \int_0^\infty \mathrm{e}^{-u - x^{2/3}\frac{2}{\pi}\int_0^\infty \frac{\cos(yux^{-2/3})(1-\mathrm{e}^{-y^{3/2}/\sqrt{2}})}{y^2}\,\mathrm{d}y}\,\mathrm{d}u \tag{17}$$

Over the range where most of the decay happens, $F(x)$ is close to a stretched exponential $F(x) \simeq \exp[-(x/a)^\beta]$ with [64] $a \simeq 1.354$ and $\beta \simeq 0.85$. Note that the asymptotic form of $F(x)$ with $\beta = 2/3$ is only valid for large x, where $F(x) < 10^{-3}$, i.e. beyond the NSE observation range.

For a finite chain with root-mean square end-to-end distance R_e in a solvent of viscosity η, the results of the Zimm model read as follows. The centre-of-mass diffusion assuming a Gaussian chain (θ-solvent) is [30]:

$$D_{\mathrm{CM}} = 0.196(0.203)k_B T/(R_e\eta) \tag{18}$$

with the modifications suggested in Ref. [30] for good solvent with $\nu = 0.6$—inserting $\nu = 1/2$ yields the Gaussian chain expression—$S(Q,t)$ is computed:

$$S(Q,t) = \sum_{m,n}^{N} \mathrm{e}^{-Q^2 D_{\mathrm{CM}} t - \frac{Q^2}{6}B(m,n,t)} \tag{19}$$

$$B(m,n,t) = |n-m|^{2\nu} l^2 + \frac{4R_e^2}{\pi^2}\sum_{p=1}^{p_{\max}} \frac{1}{p^{2\nu+1}} \cos\left(\frac{\pi pn}{N}\right)\cos\left(\frac{\pi pm}{N}\right)\left(1-\mathrm{e}^{-1/\tau_p}\right)$$

where $l^2 = (R_e^2/N^{2\nu})$ and

$$\tau_p = \frac{\eta R_e^3}{\sqrt{3\pi}k_B T}\, p^{-3\nu} \tag{20}$$

The result from Eq. (19) depends on the chain dimension R_e and the viscosity η only. For large R_e values the center-of-mass diffusion is negligible and $S(Q,t)$ corresponds to the scaling function which solely depends on η.

4.2. Not so freely joined chains

A nontrivial example of the observation of Zimm dynamics is the identification of the effect of non-flexible bonds in a kind-of 'frozen' Gaussian coil [65]. Polymers that exhibit this kind of behaviour are polynorbornenes (PN). Solution dynamics of these compared to that from a flexible linear polyisoprene (PI) as shown in Fig. 8, show considerable retardation compared to the flexible chain; whereas the scaling is well fulfilled by the PI data the PN relaxation spectra deviate significantly.

The data are explained by the assumption that Zimm modes that pertain length scales below $\simeq$105 Å are suppressed by the rigidity of the PN chain (solid lines in Fig. 8). However, the structure of the coil matches exactly the $S(Q)$ that is expected for a Gaussian coil. Thus NSE spectroscopy here clearly revealed the effect of a frozen chain conformation.

4.3. Membrane Zimm dynamics and bending modulus

Microemulsions may be viewed as composed of an interface of given total area that separates two fluids (water and 'oil') in a closely intermingled structure. The interface consists of amphiphilic surfactant molecules, the amount of

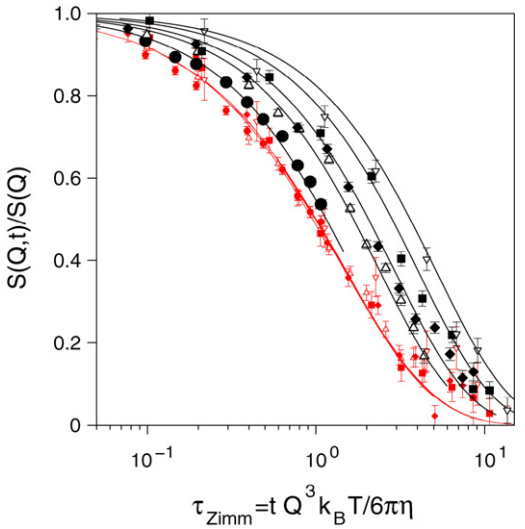

Fig. 8. Ideal Zimm scaling of a solution of linear polyisoprene ($M_w = 100$ kg/mol) in tetrahydrofurane, THF (small symbols) compared to the (semi)rigid random coil polymer, polynorbornene, large symbols: solid circle ($Q = 0.05$ Å^{-1}), open triangle upwards ($Q = 0.08$ Å^{-1}), solid diamond ($Q = 0.10$ Å^{-1}), solid square ($Q = 0.14$ Å^{-1}), open triangle downwards ($Q = 0.18$ Å^{-1}).

which determines the total available area. Depending on the composition and temperature, pressure etc. a multitude of phases with different microstructure may form. Much of the underlying physics that determines the occurrence and properties of these phases may be captured by a description of the microemulsion in terms of the Helfrich free energy [66]:

$$F_{\mathrm{el}} = \int \mathrm{d}S \left[\frac{\kappa}{2}(c_1 + c_2 - 2c_0)^2 + \bar{\kappa} c_1 c_2 \right] \tag{21}$$

where the physical description is lumped into the parameters c_0, κ and $\bar{\kappa}$. c_1 and c_2 denote the principal curvatures at each point of the membrane, c_0 is the spontaneous curvature, κ the bending rigidity and $\bar{\kappa}$ the saddle splay modulus.

The surfactant efficiency in a bicontinuous microemulsion can be enhanced by addition of a small amount of amphiphilic diblock copolymers ('boosting effect') [67–70]. It is decreased when the corresponding homopolymers are added to the water and oil respectively [71]. The effect of the diblock copolymer is explained by an increase of the stiffness of the surfactant membrane. Inversely, the homopolymers decrease the bending rigidity [71,72].

If the description Eq. (21) is interpreted in terms of the global interface structure ignoring short scale undulations of the membrane, the true local bending modulus κ_{bare} must be renormalised to lump the effect of the undulation into the parameter value. The thus renormalised value may be extracted from the diffraction intensity of the microemulsion in oil vs. water contrast and relates to the bare value by:

$$\kappa_{\mathrm{SANS}} = \kappa_{\mathrm{bare}} + k_B T \frac{\alpha}{4\pi} \ln(\psi) \tag{22}$$

where the effective length scale enters in terms of the surfactant volume fraction ψ. Different predictions exist for the factor α ranging from -1 to 3 [73–78]. One virtue emerging from the comparison of the bare κ values from NSE to the SANS results that yield renormalised parameters, is the possibility to corroborate a factor of $\alpha = 3$ [79].

The mode relaxation rate $\Omega(k)$ of the free membrane Zimm dynamics is [80]

$$\Omega(k) = \frac{\kappa k^3}{4\eta_{\mathrm{eff}}} = \frac{\kappa k^3}{2(\eta_{\mathrm{oil}} + \eta_{\mathrm{water}})} \tag{23}$$

$\eta_{\mathrm{eff}} = (\eta_{\mathrm{oil}} + \eta_{\mathrm{water}})/2$ will be considered, where η_{oil} and η_{water} are the viscosities in the corresponding water and oil sections. The mode wave vector k, however, is different from the observed neutron wave vector Q, see Eq. (26).

Zilman and Granek developed a model for the dynamics of a bicontinuous microemulsion that assumes membrane Zimm dynamics within randomly oriented planar patches of a size given by the microstructure of the bicontinuous phase [81].

$$S(Q,t) \simeq S(Q)\exp\bigl(-(\Gamma_Q t)^{\beta}\bigr) \tag{24}$$

with $\beta = 2/3$ and

$$\Gamma_Q = 0.025\gamma_\kappa \left(\frac{k_B T}{\kappa}\right)^{1/2} \frac{k_B T}{\eta} Q^3 \tag{25}$$

here, κ is the bending elasticity modulus, η the solvent viscosity, and $\gamma_\kappa \simeq 1 - 3\frac{k_B T}{4\pi\kappa}\ln(Q\xi) \longrightarrow 1$ for $\kappa \gg k_B T$.

The prefactor in Eq. (25), however, depends on additional approximations and fails to yield a good description for low κ—values as in our case. A numerical evaluation of the model avoids these approximations and yields a dynamic structure factor as described in Ref. [82]:

$$\frac{S(Q,t)}{S(Q,0)} \propto \int_0^1 \mathrm{d}\mu \int_0^{r_{\max}} \mathrm{d}r\, r\, J_0\bigl(Qr\sqrt{1-\mu^2}\bigr) \times \mathrm{e}^{-k_B T/(2\pi\kappa)Q^2\mu^2 \int_{k_{\min}}^{k_{\max}} \mathrm{d}k\, \frac{1-J_0(kr)\mathrm{e}^{-\Omega(k)t}}{k^3}} \tag{26}$$

the real space upper cutoff is $r_{\max} = \xi/\epsilon$, $k_{\min} = \pi/r_{\max}$, $k_{\max} \simeq \pi/a$ with a the surfactant molecule size and the integration variable μ is the cosine of the angle between Q and the membrane surface normal. The correlation length ξ is determined from independent SANS data from 'bulk'-contrast samples. Since the choice of the integration limits $r_{\max}$ respectively $k_{\min}$ relates to the correlation length of the surfactant membrane, but may involve an unknown factor of the order 1, the parameter ϵ was used to calibrate NSE values with SANS values for one selected sample. The resulting value of 1.13 for ϵ indicates the validity of the identification of ξ as the relevant length scale for the integrations. After fixing $\epsilon = 1.13$ the only free parameter in this equation is the bending modulus.

As an example we show results on water–decane C10E4 microemulsions with different PEP(5 kg/mol)–PEO(5 kg/mol) polymer additions. In Fig. 9 values extracted from SANS, the renormalised modulus, $\kappa_R = \kappa_{SANS}$, and the 'bare', renormalisation corrected modulus $\kappa_{SANS} - 3/(4\pi)\ln(\psi)$ are displayed. The renormalisation corrected SANS-result κ_{NSE} agrees semiquantitatively for pure and homopolymer containing microemulsions. For the microemulsions with added diblock-copolymer a slightly higher value has been obtained with NSE than with SANS. In particular, the 'bare' values as obtained by NSE as well as those derived for SANS are independent on the surfactant concentration as would be expected for a 'material' parameter of the interface membrane.

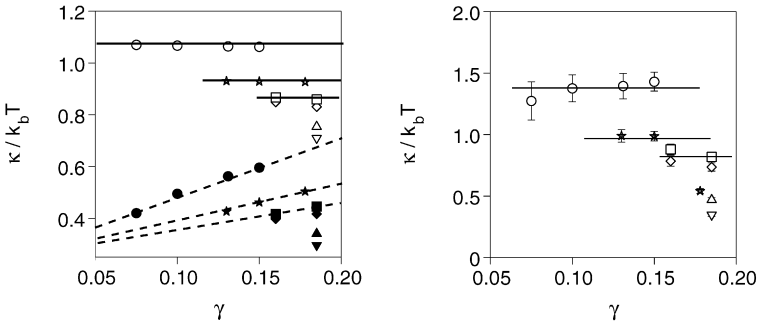

Fig. 9. Bending moduli of the water–decane–C10E4 bicontinuous microemulsion with and without added polymer. The left side shows values as extracted from SANS experiments before (filled symbols) and after renormalisation correction (empty symbols). Pure microemulsion: stars, microemulsion with 5% diblock copolymer in the added surfactant: circles, with homopolymers: squares. γ denotes the total amount of added surfactant which is inversely correlated to the structural length scale of the microemulsion. The right side compares these κ-values with those from the analysis of NSE data. The widest surfactant concentration γ regime was explored with the help of the addition of a block copolymer with a C10E4-analogous chemical structure. The boosting effect allows to start with a low concentration γ and thereby to cover a sizable concentration range. Lines are only to guide the eye.

5. Biomolecules

Biomolecules and, in particular, proteins, perform specific functions in living cells. Their function depends on the tertiary structure resulting from folding of the linear macromolecule with a defined sequence of aminoacids. The folded proteins are rather compact objects compared to a synthetic polymer in solution. They function by exposing binding sites, and eventually, by a large scale displacement of larger subunits that compose the tiny biochemical machinery. The challenge for high resolution neutron spectroscopy is the observation of these types of large scale motions. However, it is not possible to catch the protein in the act as a small calculation may illustrate. A 1% solution of a typical medium size protein contains about 10^{17} protein molecules/cm^3. The energy associated with a single step is about 10 kJ/mol. To be able to detect the associated dynamical process, its repetition rate must be comparable to the typical (relaxation) time of the motion. The latter is given by the instrumental resolution. For the NSE range, we assume that each protein should perform one transformation within a maximum time interval of 1 μs. These numbers lead to a power of consumption of chemical energy of: 1.7 kW/cm^3! It is obvious that this cannot be sustained as steady state during the days a neutron experiment takes. Therefore, one has to rely on thermal equilibrium fluctuations to investigate the motional modes of functional proteins under the assumption that the functional shape transformations are associated with the largest thermal fluctuation amplitudes of selected protein subgroups.

Still there is a certain chance to grasp the intramolecular mobilities that are relevant for the function. In a sense, proteins may be considered as molecular machines and we take the freedom to consider the analogy to, e.g. a mechanical watch. Even if the watch is not running, vigourous shaking (by the thermal bath) will reveal the presence of the balance. The analogy also tells us that too much shaking, i.e. too high temperature, will spoil this view. A denatured protein corresponds to a messy collection of gear wheels with individual mobilities that do not correspond to the state of a functioning machine.

A step towards more insight into these issues in real protein molecules is provided by the first successful detection of large scale internal motion in a protein with a molecular weight of 91 kDa (taq polymerase) by neutron spin-echo spectroscopy [83]. The taq (thermophilus aquaticus) polymerase performs nucleotid replacement in DNA repair and RNA primer removal in DNA replication [84]. To do so the protein must perform coordinated domain and subdomain motions [85,86]. An NSE experiment on a 0.8% solution of taq polymerase in D_2O has been performed.

To identify inner motions, first the centre-of-mass diffusion effects and in addition effects corresponding to the rotational diffusion of the whole aspherical body must be taken into account. This requires a good accuracy of the measured relaxation curves. So far the effects have been observed and assessed in terms of an effective diffusion coefficient $D_{\mathrm{eff}}(Q)$ obtained by fitting $S(Q,t)/S(Q) = \exp(-D_{\mathrm{eff}}Q^2 t)$ which is taken as first cumulant or initial slope determination. Effects beyond centre-of-mass diffusion D_{CM} lead to a Q-dependent modulation of $D_{\mathrm{eff}} = D_{\mathrm{CM}} + \Delta D(Q)$.

$$D_{\mathrm{eff}}(Q) = \frac{k_B T}{Q^2} \frac{\sum_{j,k} b_j b_k \langle \mathbf{Q}\cdot\mathbf{H}_{\mathbf{j},\mathbf{k}}\cdot\mathbf{Q}\exp[\mathrm{i}\mathbf{Q}\cdot(\mathbf{r_j}-\mathbf{r_k})]\rangle}{\sum_{j,k} b_j b_k \langle \exp[\mathrm{i}\mathbf{Q}\cdot(\mathbf{r}_j-\mathbf{r}_k)]\rangle} \tag{27}$$

where the mobility tensor $\mathbf{H}_{j,k}$ describes the hydrodynamic interactions and frictions and b_j denotes the scattering length of atom j. For a protein model consisting of rigid subgroups that are held together by soft potentials Eq. (27) has to be modified such that friction and hydrodynamic coupling pertain to the rigid subgroups. The summation over the atoms within each subgroup, r, s separately yields $S_{r,s}(Q)$ for the diagonal part contributions of $\mathbf{H}$ [83].

A simple approach to rationalise the NSE observations with a diagonal domain mobility taking into account only one friction parameter per subgroup (Fig. 10) is given by:

$$D_{\mathrm{eff}}(Q) = \frac{\sum_i D_i S_i(Q)}{S(Q)} \tag{28}$$

However, due to the neglect of hydrodynamic coupling between the subgroups at least the low-Q region and in particular the limit $D_{\mathrm{eff}}(Q \to 0)$ cannot be reproduced. Nevertheless part of the coupling is probably accounted for by the selection of D_i by a fitting procedure. The modulation at intermediate Q then is an indication of the proper subgroup sectioning.

Application of Eq. (28) allowed the identification of the mobile subgroups in Ref. [83]. A more detailed analysis requires the inclusion of hydrodynamic coupling and the extension of the analysis beyond the effective initial slope, i.e. the experimental analysis of deviations of $S(Q,t)$ from simple exponential behaviour. Fig. 10 displays the taq-molecule (as inferred from the crystal structure (Protein Data Bank ID code 1TAQ)) [87,88] where three subdomains

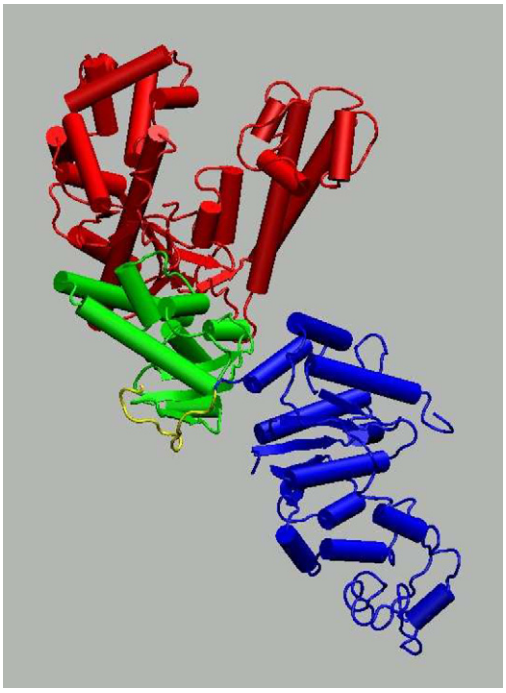

Fig. 10. Taq structure with color coding of the loosely coupled domains.

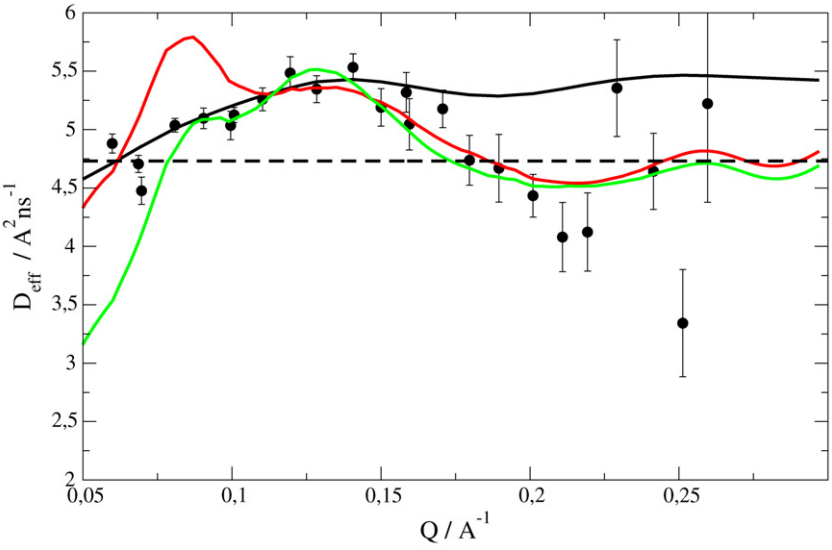

Fig. 11. Effective diffusion constant of Taq in aqueous solution as obtained from initial slope (i.e. slope of the relaxation curves in the range $1\ \text{ns} \leqslant \tau \leqslant 30\ \text{ns}$). The red and green lines correspond to two and three domain models respectively.

are indicated (color) which have been identified with the help of harmonic vibration analysis [89]. The $D_{\text{eff}}(Q)$ data were derived by fitting single exponentials to the first 30 ns of the NSE data that represent $S(Q,t)/S(Q) = \exp(-Q^2 D_{\text{eff}}(Q)t)$. Fig. 11 displays these values (symbols) in comparison with different models. The black line is obtained with parameters from HYDROPRO [90–92] and assumes rigid body rotation of the whole molecule. The red and green lines correspond to two and three domain models of the protein, respectively. Whereas the rigid body rotation describes the data up to $Q \simeq 0.15$ Å quantitatively, beyond that, deviations are observed that are compatible with the three domain model of Fig. 10.

Thus the experiment was successful in identifying dynamic effects due to internal domain motions in taq and to corroborate the sectioning into domains as inferred from harmonic analysis. However, the accuracy and time domain of the experiment was not yet sufficient to identify the extension of the 'initial slope' dominated range and to see deviations from single exponential decay. Therefore further experiments would be needed to infer spring constants and motional amplitudes. Also, a full hydrodynamic description should improve the computed $D_{\mathrm{eff}}(Q)$ behaviour in the low Q-regime.

6. Conclusions

We have given an overview of the high resolution neutron spectrometers, NSE and BSS that are most important for the investigation of dynamics in soft matter systems on a molecular scale. The use of these instruments is illustrated by a selection of examples showing the type of information that may be obtained and how this may be done. The application ranges from the molecular basics of polymer melt rheology to internal dynamics of proteins. Future trends that currently can be anticipated will shift more emphasis towards biological systems, e.g. protein dynamics and (nano) composite soft matter. The 'classical' molecular rheology will move from linear homogeneous polymers towards new molecular architectures and blends or mixtures with fillers, keeping its main goal to relate the microscopic dynamics to viscoelastic properties. Microemulsions will certainly remain an active field in particular for NSE spectroscopy where also here the investigation of the role of additives (e.g. cosurfactants, amphiphilic polymers of different architecture) on various phases will prevail. The behaviour of polymer melts, solutions and microemulsions in microporous environments as well as application of pressure, flow fields and other external forces may open further new fields. Whereas faster dynamics of proteins or water bound to proteins in powders have been investigated with neutron scattering since many years, the observation of large scale domain motion has only been tackled recently. Due to improvements in computing power and molecular dynamics techniques simulations start to reach the ns-timescale that matches the range of NSE spectroscopy. The coming years will show whether by these means functional domain motions can be investigated by looking at corresponding equilibrium Brownian domain fluctuations with NSE and BSS. Similarly intrinsically unfolded proteins (IUP) may become another interesting subject, with the challenge to understand the structure of the large non-folded strands in these molecules. Combination of NSE and BSS may become vital to discriminate dynamics of coherent scattering and contributions from incoherent ones. Gels with functions, made from biomolecules or used to modify the diffusion or interactions of hosted biomolecules or new inventions as e.g. the 'sliding' gels with rotaxane rings as mobile links between polymer chains also deserve more focus.

Appendix A. Approximations

The following approximations may be helpful to perform a quick comparison of data to a Rouse prediction. The scaling function $F(x)$, Eq. (12) may be represented with an accuracy of $\simeq 10^{-3}$ by the sum of 3 stretched exponentials $F(x) \simeq \sum_{i=1}^{3} a_i \exp[(x/x_i)^{\beta_i}]$ with $a_{1\ldots3} = (0.5871, 0.3282, 0.08475)$, $x_{1\ldots3} = (4.112, 1.780, 0.5282)$ and $\beta_{1\ldots3} = (0.7484, 0.8973, 1.0)$. If 2% accuracy are sufficient an even simpler approximation $F(x) \simeq \exp[-(x/2.7)^{0.7}]$ may be used. A similar approximation for the local reptation function (=Rouse relaxation in and along a tube) $F(x) = \exp(x)\mathrm{erfc}(x)$ is obtained with: $a_{1\ldots3} = (0.4794, 0.3836, 0.1380)$, $x_{1\ldots3} = (0.4282, 3.524, 91.50)$ and $\beta_{1\ldots3} = (0.4774, 0.4204, 0.3160)$.

References

[1] R.G. Kirste, J. Schelten, W.A. Kruse, Determination of radius of gyration of polymethylmethacrylate in glass state by neutron-diffraction, Makromolekulare Chemie 162 (1972) 299–303.
[2] H. Benoit, D. Decker, R. Duplessix, C. Picot, P. Rempp, Characterization of polystyrene networks by small-angle neutron-scattering, Journal of Polymer Science Part B—Polymer Physics 14 (1976) 2119–2128.
[3] J.M. Guenet, C. Picot, H. Benoit, Chain conformation of isotactic polystyrene in the bulk amorphous state as revealed by small-angle neutron-scattering, Macromolecules 12 (1979) 86–90.
[4] B. Alefeld, M. Birr, A. Heideman, A new high resolution neutron crystal spectrometer and its application, Naturwissenschaften 56 (1969) 410.
[5] M. Birr, A. Heideman, B. Alefeld, Neutron crystal spectrometer with extremely high energy resolution, Nuclear Instruments & Methods 95 (1971) 435.

[6] J. Schelten, B. Alefeld, in: R. Scherm, H.H. Stiller (Eds.), Proceedings on the Workshop on Neutron Scattering Instrumentation for SNQ.
[7] O. Kirstein, T. Kozielewski, M. Prager, D. Richter, Status of the high-flux backscattering spectrometer RSSM for the FRM-II reactor in Munich, Applied Physics A—Materials Science & Processing 74 (2002) S133–S135.
[8] A. Meyer, R.M. Dimeo, P.M. Gehring, D.A. Neumann, The high-flux backscattering spectrometer at the NIST Center for Neutron Research, Review of Scientific Instruments 74 (2003) 2759–2777.
[9] F. Mezei, Neutron spin-echo—new concept in polarized thermal-neutron techniques, Zeitschrift Fur Physik 255 (1972) 146.
[10] F. Mezei (Ed.), Neutron Spin Echo, Lecture Notes in Physics, vol. 128, Springer, Berlin, Heidelberg, New York, 1980.
[11] F. Mezei, C. Pappas, T. Gutberlet (Eds.), Neutron Spin Echo Spectroscopy, Lecture Notes in Physics, vol. 601, Springer, Berlin, Heidelberg, New York, 2003.
[12] E.L. Hahn, Spin echoes, Physical Review 80 (1950) 580–594.
[13] P. Schleger, B. Alefeld, J.F. Barthelemy, G. Ehlers, B. Farago, P. Giraud, C. Hayes, A. Kollmar, C. Lartigue, F. Mezei, D. Richter, The long-wavelength neutron spin-echo spectrometer IN15 at the Institut Laue-Langevin, Physica B 241 (1997) 164–165.
[14] B. Farago, Recent neutron spin-echo developments at the ILL (IN11 and in15), Physica B 268 (1999) 270–276.
[15] M. Monkenbusch, R. Schatzler, D. Richter, The Julich neutron spin-echo spectrometer—Design and performance, Nuclear Instruments & Methods in Physics Research Section A—Accelerators Spectrometers Detectors and Associated Equipment 399 (1997) 301–323.
[16] N. Rosov, S. Rathgeber, M. Monkenbusch, Neutron spin echo spectroscopy at the NIST Center for Neutron Research, Scattering from Polymers 739 (2000) 103–116.
[17] T. Takeda, S. Komura, H. Seto, M. Nagai, H. Kobayashi, E. Yokoi, T. Ebisawa, S. Tasaki, C.M.E. Zeyen, Y. Ito, S. Takahashi, H. Yoshizawa, Neutron spin-echo spectrometer at jrr-3m, Physica B 213 (1995) 863–865.
[18] T. Takeda, H. Seto, Y. Kawabata, D. Okuhara, T. Krist, C.M.E. Zeyen, I.S. Anderson, P. Hoghoj, M. Nagao, H. Yoshizawa, S. Komura, T. Ebisawa, S. Tasaki, M. Monkenbusch, Improvement of neutron spin echo spectrometer at C2-2 of jrr3m, Journal of Physics and Chemistry of Solids 60 (1999) 1599–1601.
[19] M. Ohl, M. Monkenbusch, D. Richter, Neutron spin-echo spectrometer development for spallation sources, Physica B—Condensed Matter 335 (2003) 153–156.
[20] M. Ohl, M. Monkenbusch, D. Richter, C. Pappas, K. Lieutenant, T. Krist, G. Zsigmond, F. Mezei, The high-resolution neutron spin-echo spectrometer for the SNS with $\tau >= 1$ μs, Physica B—Condensed Matter 350 (2004) 147–150.
[21] M. Ohl, M. Monkenbusch, T. Kozielewski, B. Laatsch, C. Tiemann, D. Richter, Correction elements for ultra-high resolution NSE spectrometer, Physica B—Condensed Matter 356 (2005) 234–238.
[22] C. Pappas, R. Kischnik, F. Mezei, Wide angle NSE: the spectrometer SPAN at BENSC, Physica B 297 (2001) 14–17.
[23] R. Golub, R. Gahler, A neutron resonance spin-echo spectrometer for quasi-elastic and inelastic-scattering, Physics Letters A 123 (1987) 43–48.
[24] M. Koppe, M. Bleuel, R. Gahler, R. Golub, P. Hank, T. Keller, S. Longeville, U. Rauch, J. Wuttke, Prospects of resonance spin echo, Physica B—Condensed Matter 266 (1999) 75–86.
[25] S. Longeville, Neutron spin echo spectrometry with zero field or by resonance, Journal de Physique IV 10 (2000) 59–75.
[26] S. Dellerue, A. Petrescu, J.C. Smith, S. Longeville, M.C. Bellissent-Funel, Collective dynamics of a photosynthetic protein probed by neutron spin-echo spectroscopy and molecular dynamics simulation, Physica B 276 (2000) 514–515.
[27] S. Longeville, W. Doster, G. Kali, Myoglobin in crowded solutions: structure and diffusion, Chemical Physics 292 (2003) 413–424.
[28] P.E. Rouse, A theory of the linear viscoelastic properties of dilute solutions of coiling polymers, Journal of Chemical Physics 21 (1953) 1272–1280.
[29] P.G. De Gennes, Quasi-elastic scattering of neutrons by dilute polymer solutions. I. Free-draining limit, Physics—New York 3 (1967) 37.
[30] M. Doi, S.F. Edwards, The Theory of Polymer Dynamics, International Series of Monographs on Physics, vol. 73, Oxford University Press, Oxford, 1994.
[31] Dubois Violette, P.G. De Gennes, Quasi-elastic scattering by dilute ideal polymer solutions. 2. Effects of hydrodynamic interactions, Physics—New York 3 (1967) 181.
[32] F. Bueche, Entanglements of polymer chains, Journal of Polymer Science 25 (1957) 243–245.
[33] R.S. Porter, J.F. Johnson, Entanglement concept in polymer systems, Chemical Reviews 66 (1966) 1.
[34] P.G. De Gennes, Dynamics of entangled polymer-solutions. 1. Rouse model, Macromolecules 9 (1976) 587–593.
[35] P.G. De Gennes, Coherent scattering by one reptating chain, Journal de Physique 42 (1981) 735–740.
[36] P.G. De Gennes, L. Leger, Dynamics of entangled polymer-chains, Annual Review of Physical Chemistry 33 (1982) 49–61.
[37] M. Doi, S.F. Edwards, Dynamics of concentrated polymer systems. 1. Brownian-motion in equilibrium state, Journal of The Chemical Society—Faraday Transactions II 74 (1978) 1789–1801.
[38] M. Doi, S.F. Edwards, Dynamics of concentrated polymer systems. 2. Molecular-motion under flow, Journal of The Chemical Society—Faraday Transactions II 74 (1978) 1802–1817.
[39] M. Doi, S.F. Edwards, Dynamics of concentrated polymer systems. 3. Constitutive equation, Journal of The Chemical Society—Faraday Transactions II 74 (1978) 1818–1832.
[40] M. Doi, S.F. Edwards, Dynamics of rod-like macromolecules in concentrated-solution. 2, Journal of The Chemical Society—Faraday Transactions II 74 (1978) 918–932.
[41] M. Doi, S.F. Edwards, Dynamics of rod-like macromolecules in concentrated-solution. 1, Journal of The Chemical Society—Faraday Transactions II 74 (1978) 560–570.
[42] M. Doi, S.F. Edwards, Dynamics of concentrated polymer systems. 4. Rheological properties, Journal of The Chemical Society—Faraday Transactions II 75 (1979) 38–54.
[43] D. Richter, L. Willner, A. Zirkel, B. Farago, L.J. Fetters, J.S. Huang, Polymer motion at the crossover from rouse to reptation dynamics, Macromolecules 27 (1994) 7437–7446.

[44] D. Richter, B. Ewen, B. Farago, T. Wagner, Microscopic dynamics and topological constraints in polymer melts—a neutron-spin-echo study, Physical Review Letters 62 (1989) 2140–2143.
[45] D. Richter, R. Butera, L.J. Fetters, J.S. Huang, B. Farago, B. Ewen, Entanglement constraints in polymer melts—a neutron spin-echo study, Macromolecules 25 (1992) 6156–6164.
[46] P. Schleger, B. Farago, C. Lartigue, A. Kollmar, D. Richter, Clear evidence of reptation in polyethylene from neutron spin-echo spectroscopy, Physical Review Letters 81 (1998) 124–127.
[47] T.C.B. McLeish, Tube theory of entangled polymer dynamics, Advances in Physics 51 (2002) 1379–1527.
[48] D. Richter, B. Farago, R. Butera, L.J. Fetters, J.S. Huang, B. Ewen, On the origins of entanglement constraints, Macromolecules 26 (1993) 795–804.
[49] A. Wischnewski, D. Richter, M. Monkenbusch, L. Willner, B. Farago, G. Ehlers, P. Schleger, Reptation in polyethylene-melts with different molecular weights, Physica B 276 (2000) 337–338.
[50] A. Wischnewski, M. Monkenbusch, L. Willner, D. Richter, G. Kali, Direct observation of the transition from free to constrained single-segment motion in entangled polymer melts, Physical Review Letters 90 (2003) 058302.
[51] A. Wischnewski, M. Monkenbusch, L. Willner, D. Richter, A.E. Likhtman, T.C.B. McLeish, B. Farago, Molecular observation of contour-length fluctuations limiting topological confinement in polymer melts, Physical Review Letters 88 (2002) 058301.
[52] A.E. Likhtman, T.C.B. McLeish, Quantitative theory for linear dynamics of linear entangled polymers, Macromolecules 35 (2002) 6332–6343.
[53] N. Clarke, T.C.B. Mcleish, The dynamic structure factor of a star polymer in a concentrated-solution, Macromolecules 26 (1993) 5264–5266.
[54] M. Zamponi, M. Monkenbusch, L. Willner, A. Wischnewski, B. Farago, D. Richter, Contour length fluctuations in polymer melts: A direct molecular proof, Europhysics Letters 72 (2005) 1039–1044.
[55] S.T. Milner, T.C.B. McLeish, Reptation and contour-length fluctuations in melts of linear polymers, Physical Review Letters 81 (1998) 725–728.
[56] M. Zamponi, A. Wischnewski, M. Monkenbusch, L. Willner, D. Richter, A.E. Likhtman, G. Kali, B. Farago, Molecular observation of constraint release in polymer melts, Physical Review Letters 96 (2006) 238302.
[57] A.E. Likhtman, Single-chain slip-link model of entangled polymers: Simultaneous description of neutron spin-echo, rheology, and diffusion, Macromolecules 38 (2005) 6128–6139.
[58] W. Paul, G.D. Smith, D.Y. Yoon, B. Farago, S. Rathgeber, A. Zirkel, L. Willner, D. Richter, Chain motion in an unentangled polyethylene melt: A critical test of the rouse model by molecular dynamics simulations and neutron spin echo spectroscopy, Physical Review Letters 80 (1998) 2346–2349.
[59] G.D. Smith, W. Paul, D.Y. Yoon, A. Zirkel, J. Hendricks, D. Richter, H. Schober, Local dynamics in a long-chain alkane melt from molecular dynamics simulations and neutron scattering experiments, Journal of Chemical Physics 107 (1997) 4751–4755.
[60] G.D. Smith, W. Paul, M. Monkenbusch, L. Willner, D. Richter, X.H. Qiu, M.D. Ediger, Molecular dynamics of a 1,4-polybutadiene melt. Comparison of experiment and simulation, Macromolecules 32 (1999) 8857–8865.
[61] G.D. Smith, W. Paul, M. Monkenbusch, D. Richter, A comparison of neutron scattering studies and computer simulations of polymer melts, Chemical Physics 261 (2000) 61–74.
[62] G.D. Smith, W. Paul, M. Monkenbusch, D. Richter, On the non-Gaussianity of chain motion in unentangled polymer melts, Journal of Chemical Physics 114 (2001) 4285–4288.
[63] B.H. Zimm, Dynamics of polymer molecules in dilute solution—viscoelasticity, flow birefringence and dielectric loss, Journal of Chemical Physics 24 (1956) 269–278.
[64] D. Richter, M. Monkenbusch, A. Arbe, J. Colmenero, Neutron spin echo in polymer systems, Neutron Spin Echo in Polymer Systems 174 (2005) 1–221.
[65] M. Monkenbusch, J. Allgaier, D. Richter, J. Stellbrink, L.J. Fetters, A. Greiner, Nonflexible coils in solution: A neutron spin-echo investigation of alkyl-substituted polynorbornenes in tetrahydrofuran, Macromolecules 39 (2006) 9473–9479.
[66] W. Helfrich, Elastic properties of lipid bilayers—theory and possible experiments, Zeitschrift Fur Naturforschung C—A Journal of Biosciences C 28 (1973) 693–703.
[67] B. Jakobs, T. Sottmann, R. Strey, J. Allgaier, L. Willner, D. Richter, Amphiphilic block copolymers as efficiency boosters for microemulsions, Langmuir 15 (1999) 6707–6711.
[68] H. Endo, M. Mihailescu, M. Monkenbusch, J. Allgaier, G. Gompper, D. Richter, B. Jakobs, T. Sottmann, R. Strey, I. Grillo, Effect of amphiphilic block copolymers on the structure and phase behavior of oil–water–surfactant mixtures, Journal of Chemical Physics 115 (2001) 580–600.
[69] H. Endo, J. Allgaier, M. Mihailescu, M. Monkenbusch, G. Gompper, D. Richter, B. Jakobs, T. Sottmann, R. Strey, Amphiphilic block copolymers as efficiency boosters in microemulsions: a SANS investigation of the role of polymers, Applied Physics A—Materials Science & Processing 74 (2002) S392–S395.
[70] M. Mihailescu, M. Monkenbusch, H. Endo, J. Allgaier, G. Gompper, J. Stellbrink, D. Richter, B. Jakobs, T. Sottmann, B. Farago, Dynamics of bicontinuous microemulsion phases with and without amphiphilic block-copolymers, Journal of Chemical Physics 115 (2001) 9563–9577.
[71] D. Byelov, H. Frielinghaus, O. Holderer, J. Allgaier, D. Richter, Microemulsion efficiency boosting and the complementary effect. 1. Structural properties, Langmuir 20 (2004) 10433–10443.
[72] A. Hanke, E. Eisenriegler, S. Dietrich, Polymer depletion effects near mesoscopic particles, Physical Review E 59 (1999) 6853–6878.
[73] L. Peliti, S. Leibler, Effects of thermal fluctuations on systems with small surface-tension, Physical Review Letters 54 (1985) 1690–1693.
[74] W. Helfrich, Effect of thermal undulations on the rigidity of fluid membranes and interfaces, Journal de Physique 46 (1985) 1263–1268.
[75] W.C. Cai, T.C. Lubensky, Covariant hydrodynamics of fluid membranes, Physical Review Letters 73 (1994) 1186–1189.
[76] G. Gompper, D.M. Kroll, Random surface discretizations and the renormalization of the bending rigidity, Journal de Physique I 6 (1996) 1305–1320.

[77] H.A. Pinnow, W. Helfrich, Effect of thermal undulations on the bending elasticity and spontaneous curvature of fluid membranes, European Physical Journal E 3 (2000) 149–157.
[78] G. Gompper, H. Endo, M. Mihailescu, J. Allgaier, M. Monkenbusch, D. Richter, B. Jakobs, T. Sottmann, R. Strey, Measuring bending rigidity and spatial renormalization in bicontinuous microemulsions, Europhysics Letters 56 (2001) 683–689.
[79] O. Holderer, H. Frielinghaus, D. Byelov, M. Monkenbusch, J. Allgaier, D. Richter, Dynamic properties of microemulsions modified with homopolymers and diblock copolymers: The determination of bending moduli and renormalization effects, Journal of Chemical Physics 122 (2005) 094908.
[80] T. Schilling, O. Theissen, G. Gompper, Dynamics of the swollen lamellar phase, European Physical Journal E 4 (2001) 103–114.
[81] A.G. Zilman, R. Granek, Undulations and dynamic structure factor of membranes, Physical Review Letters 77 (1996) 4788–4791.
[82] M. Mihailescu, M. Monkenbusch, H. Endo, J. Allgaier, G. Gompper, J. Stellbrink, D. Richter, B. Jakobs, T. Sottmann, B. Farago, Dynamics of bicontinuous microemulsion phases with and without amphiphilic block-copolymers, Journal of Chemical Physics 115 (2001) 9563–9577.
[83] Z.M. Bu, R. Biehl, M. Monkenbusch, D. Richter, D.J.E. Callaway, Coupled protein domain motion in Taq polymerase revealed by neutron spin-echo spectroscopy, Proceedings of The National Academy of Sciences of The United States of America 102 (2005) 17646–17651.
[84] A. Kornberg, T.A. Baker, DNA Replication, Freeman, San Francisco, 1992.
[85] V. Lyamichev, M.A.D. Brow, J.E. Dahlberg, Structure-specific endonucleolytic cleavage of nucleic-acids by eubacterial DNA-polymerases, Science 260 (1993) 778–783.
[86] G. Zaccai, Biochemistry—How soft is a protein? A protein dynamics force constant measured by neutron scattering, Science 288 (2000) 1604–1607.
[87] Y. Kim, S.H. Eom, J.M. Wang, D.S. Lee, S.W. Suh, T.A. Steitz, Crystal-structure of thermus-aquaticus DNA-polymerase, Nature 376 (1995) 612–616.
[88] S.H. Eom, J.M. Wang, T.A. Steitz, Structure of Taq polymerase with DNA at the polymerase active site, Nature 382 (1996) 278–281.
[89] D. Van der Spoel, E. Lindahl, B. Hess, G. Groenhof, A.E. Mark, H.J.C. Berendsen, Gromacs: Fast, flexible, and free, Journal of Computational Chemistry 26 (2005) 1701–1718.
[90] B. Carrasco, J.G. de la Torre, Hydrodynamic properties of rigid particles: Comparison of different modeling and computational procedures, Biophysical Journal 76 (1999) 3044–3057.
[91] B. Carrasco, J.G. de la Torre, Improved hydrodynamic interaction in macromolecular bead models, Journal of Chemical Physics 111 (1999) 4817–4826.
[92] J.G. de la Torre, M.L. Huertas, B. Carrasco, Calculation of hydrodynamic properties of globular proteins from their atomic-level structure, Biophysical Journal 78 (2000) 719–730.